catalysts

MDPI

Article

Sterical Self-Consistency of Carbonaceous Nanopolyhedra Triggered by Introduced CNTs to Optimize ORR Performance

Yuanhui Zuo [1,*], Yanlong Tang [1], Huancong Shi [2], Shijian Lu [3] and Paitoon Tontiwachwuthikul [4]

[1] Research Institute of Fudan University in Ningbo, Ningbo 315327, China
[2] Huzhou Institute of Zhejiang University, Huzhou 313000, China; hcshi@usst.edu.cn
[3] Carbon Neutrality Institute, China University of Mining and Technology, Xuzhou 221006, China; lushijian@cumt.edu.cn
[4] Clean Energy Technology Research Institute (CETRI), Faculty of Engineering and Applied Science, University of Regina, Regina, SK S4S 0A2, Canada; paitoon@uregina.ca
* Correspondence: zuo_yuanhui@fudan.edu.cn

Abstract: The electrocatalyst of oxygen reduction reactions is one of the basic components of a fuel cell. In addition to costly Pt/C benchmark catalysts, cost-effective carbon-based catalysts have received the most attention. Enormous efforts have been dedicated to trade off the catalyst performance against the economic benefit. Optimizing composition and/or structure is a universal strategy for improving performance, but it is typically limited by tedious synthesis steps. Herein, we have found that directly introducing CNT into MOF-derived carbonaceous nanopolyhedra, i.e., introduced carbon nanotubes (CNTs) penetrated porous nitrogen-doped carbon polyhedra (NCP) dotted with cobalt nanoparticles (denoted as CNTs-Co@NCP), can optimize the catalytic activity, stability, and methanol tolerance. The hierarchical architecture combines the 0D/1D/3D Co/CNT/NCP interfaces and 1D/3D CNT/NCP junctions with the frameworks with a greatly exposed active surface, strengthened mass transport kinetics, stereoscopic electrical conductivity networks and structural robustness. The sterical self-consistency of MOF-self-assembly triggered by introduced CNTs demonstrates tactful ORR electrocatalytic activity regulation. Eventually, the CNTs-Co@NCP showed a half-wave potential ($E_{1/2}$) of 0.86 V and a diffusion-limited current density (J_L) of 5.94 mA/cm^2 in alkaline electrolyte. The CNTs-Co@NCP was integrated into the cathode of a direct methanol fuel cell (DMFC) with an anion-exchange membrane, and an open-circuit voltage (OCV) of 0.93 V and a high power density of 46.6 mW cm^{-2} were achieved. This work successfully developed a catalyst with competitive ORR performance through plain parameter fine-tuning without complex material design.

Keywords: oxygen reduction reaction; sterical self-consistency; carbon-based catalyst; stereoscopic conductive network; DMFC

Citation: Zuo, Y.; Tang, Y.; Shi, H.; Lu, S.; Tontiwachwuthikul, P. Sterical Self-Consistency of Carbonaceous Nanopolyhedra Triggered by Introduced CNTs to Optimize ORR Performance. *Catalysts* **2023**, *13*, 1307. https://doi.org/10.3390/catal13091307

Academic Editor: Leonarda Liotta

Received: 21 August 2023
Revised: 12 September 2023
Accepted: 18 September 2023
Published: 19 September 2023

1. Introduction

The pressing energy dilemma and environmental issues spawn a rapid development of various sustainable energy technologies [1]. Electrochemical energy transformation technologies, including fuel cells, have been adopted for desired performance and renewable energy sources. Oxygen reduction reaction (ORR) is a significant part of the electrochemical energy equipment [2,3]. ORR, a dynamic slow process, involves multi-electron and multi-step reactions. The Pt/C is a benchmark catalyst and has high activity for ORR, but its scarcity and poor steadiness severely restrict its extensive application. Thus, enormous efforts have been dedicated to trade off the catalytic performance against the economic benefits. Noble-metal-free carbon-based catalysts have received growing attention owning to the adequate reserve and potential for accelerating the sluggish kinetics of ORR through cost-effective and easy-to-operate strategies [4]. With unique features including high surface area, tailorability, and different constructions, metal-organic frameworks (MOFs) have been regarded as promising precursors and self-sacrificial templates for preparing

carbon-based nanostructured porous catalysts, as well as featured periodic network structures. Amorphous carbon construction from zeolite imidazolate framework-8 (ZIF-8) via pyrolysis showed great surface area and high porosity but less advantageous electronic conductivity. Correspondingly, the conversion of ZIF-67 with less surface area than ZIF-8 to a greatly graphitic carbon construction can be made. The carbonaceous derivatives pyrolyzed from the precursors combined ZIF-8 with ZIF-67 exhibit good ORR electrocatalytic activity with characteristics such as a great level of graphitic carbon, generation of Co-N_x moiety, and high surface area. For example, the reported core–shell ZIF-67@ZIF-8 or ZIF-8@ZIF-67 structures were employed as sacrifice templates to prepare active ORR electrocatalysts [5–14]. A functional electrocatalyst with a core–shell structure which combined the unique individual nature of pyrolyzed ZIF-8 and ZIF-67 was designed by Wang et al. Purposefully by a seed-mediated development method adopting a hydrothermal approach. The graphitic carbon shell on nitrogen-doped carbon results in high activities towards oxygen reduction owing to the potential synergistic interaction [5]. In addition, some other designable ZIF-8/67-derived catalysts were also exploited to balance the ORR electrocatalytic activity and the economic cost [4,15–27]. Peng et al. prepared a highly efficient ORR electrocatalyst, i.e., Co_9S_8 nanoparticles embedded in N, S co-doped hollow carbon nanosheets, which was realized by carbonizing ZIF-67/ZIF-8 nanosheet template and partially vulcanizing. Overall, on the one hand, the reported ZIF-8/ZIF-67-based work needs tedious synthesis processes. On the other hand, the structural stability is still insufficient. As it is a significant issue, the durability of ORR catalysts cannot be neglected in practical use. Carbon nanotubes (CNTs) with well-graphitized closed structures have few dangling bonds and defects, providing them with natural advantages in steadiness and resistance to corrosion in different electrolytes. Li et al. proposed a dual-phasic carbon nanoarchitecture for ORR by directly introducing CNTs into ZIF-67 along with a chemical modification process [19]. Welding CNTs into ZIF-8/67-derived carbonaceous nanopolyhedra, especially sp^2-hybridized carbon, to generate a cross-linking structure may be an efficient method to enhance the overall properties of the assembled structures [28]. It can be conceived that through building the hollow walls in the porous carbon polyhedra, the diffusion resistance can be decreased further to strengthen the accessibility of active sites and further drive the catalytic performance.

Herein, the hybrid catalyst viz. carbon nanotubes (CNTs) penetrated porous nitrogen-doped carbon polyhedra (NCP) dotted with cobalt nanoparticles (denoted as CNTs-Co@NCP) was fabricated by employing one-pot synthesized ZIF-8/67/CNTs as precursor without any extra embellishment. In the pyrolysis, the expected carbon composite CNT/NCP can inherit the intertwined 1D/3D architecture of ZIF-8/67/CNTs, while the pore walls of ZIF-8/67 realize a solid-to-hollow change with the evaporation of metal Zn and the generation of Co nanoparticles. The 1D/3D porous skeleton of CNTs-Co@NCP can drive long-scope mass transfer, meanwhile, the 0D/1D/3D Co/CNT/NCP interfaces can promote local accessibility of active sites. The CNTs-Co@NCP catalyst exhibited significantly enhanced catalytic activity and stability for ORR. It is worth noting that the sterical self-consistency of MOF-self-assembly triggered by introduced CNTs has proved tactful ORR electrocatalytic activity regulation owing to the size effect and adaptive spatial distribution. The introduction of CNTs increases the exposure of the active sites buried in thick polyhedra and the accessibility to reaction substrates. An alkaline DMFC assembled with CNTs-Co@NCP in the cathode exhibits an open-circuit voltage (OCV) of 0.93 V and a maximum power density of 46.6 mW cm^{-2}, which means a catalyst with competitive ORR performance was successfully developed through plain parameter fine-tuning without complex material design.

2. Results and Discussion

2.1. Preparation and Characterization

Highly conductive CNTs-Co@NCP was prepared using a simple process including physical stirring and following pyrolysis reduction [29]. The fabrication process is schemat-

ically depicted in Scheme 1, as well as the influencing factors on the performance of electrocatalysts. Firstly, some CNTs were added into a homogenous methanol solution containing cobalt nitrate hexahydrate and zinc nitrate hexahydrate under physical stirring. Then, 2-methylimidazole methanol solution was quickly injected into the above system and then the ZIF-8/67/CNTs precursor was produced. After pyrolysis, the CNTs firmly penetrate and string the carbonized polyhedra derived from bimetallic ZIF-8/67. It was found that the composition, pyrolysis temperature, and CNTs mass had an impact on the catalyst performance; the fluctuation of CNTs mass leads to conspicuous size effects.

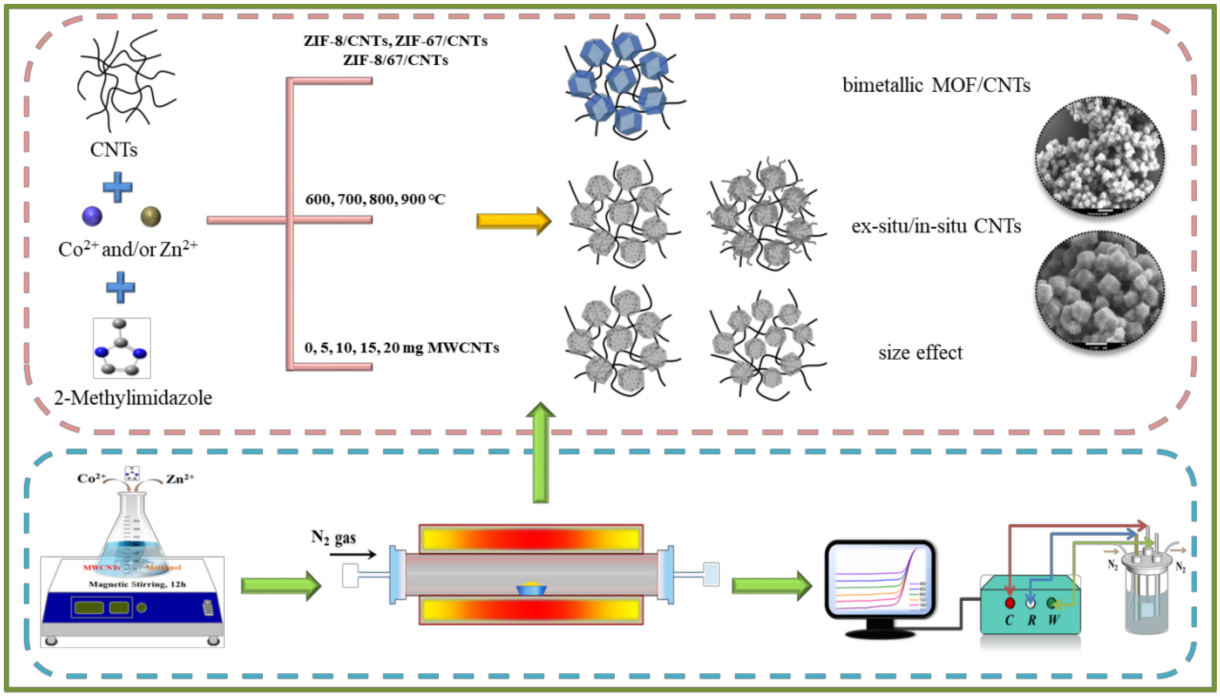

Scheme 1. Schematic diagram of the synthesis procedure and the influencing parameters toward CNTs-Co@NCP electrocatalytic performance.

Figure 1 shows the color contrast photographs of samples prepared under different conditions. As shown in Figure 1a, different composition leads to significant color difference, i.e., ZIF-8/CNTs (gray), ZIF-67/CNTs (deep purple), ZIF-8/67/CNTs (grayish purple), and ZIF-8/67 (bright purple). In addition, as the amount of CNTs increases in ZIF-8/67/CNTs, the color becomes darker (Figure 1b). The morphological changes of precursors after carbonization can be visualized from the scanning electron microscope (SEM) images. Pyrolytic samples with different composition (ration: 20 mg CNTs, 900 °C pyrolysis temperature) are labeled as C-Z8/C, C-Z67/C, C-Z8/67/C, and C-Z8/67 (Figures 2 and 3a). The CNTs in C-Z8/C can be clearly observed from Figure 2a (marked out with yellow arrows). The broken carbon particles derived from ZIF-8 suffered from configurational decomposition because of the Zn evaporation at large pyrolysis temperature. As shown in Figure 2b,d, the C-Z67/C and C-Z8/67 nanostructures exhibit irregular morphology after carbonization which differs from the reported general results toward the ZIF-67 derivate, indicating that the introduced CNTs and the pyrolysis catalysis affect the final structure. However, the C-Z8/67/C presents uniform size and regular morphology, which owns to the synergistic effect, as shown in Figure 2c. Remarkably, the specially designed system (i.e., bimetallic MOFs coupled with introduced CNTs) shows excellent steric hindrance roles of size and optimally structural stability compared to other catalysts, which proves the rationality of composition and structure. Subsequently, the effect of pyrolysis temperature was studied further, the prepared samples are marked as C-Z8/67/C-600, C-Z8/67/C-700, C-Z8/67/C-800, and C-Z8/67/C-900. The feature of the C-Z8/67/C prepared at different pyrolysis temperatures does not differ much (Figure 4). It can be observed that when the temperature

reaches 900 °C, the profile of C-Z8/67/C-900 becomes a bit blurred owning to the in situ generated short CNTs. At low pyrolysis temperatures, the in situ catalytic CNTs cannot be observed obviously. In addition, subsequent experiments demonstrated that the influence of in situ CNTs on the electrocatalytic performance is negligible, compared with the introduced CNTs. Furthermore, the effect of different mass of CNTs on the catalyst activity was investigated, and obvious size effects can be clearly and intuitively seen from Figure 5, such as the greater amount of CNTs and the smaller size of polyhedra, which is caused by the sterical self-consistence. Through the investigation of electrocatalytic performance, we have proven that the ZIF-8/67/CNTs-derived catalyst CNTs-Co@NCP prepared with 15 mg CNTs under 800 °C exhibited the best ORR electrocatalytic activity.

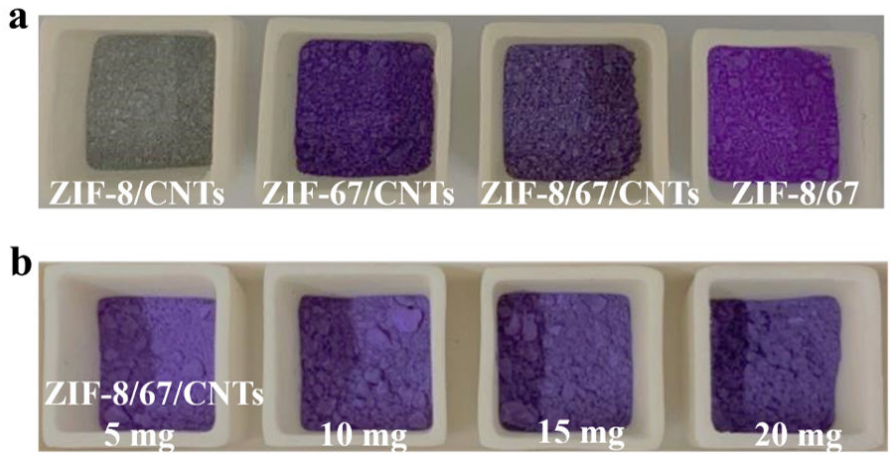

Figure 1. Optical photographs of samples with different (**a**) composition, and (**b**) CNTs mass.

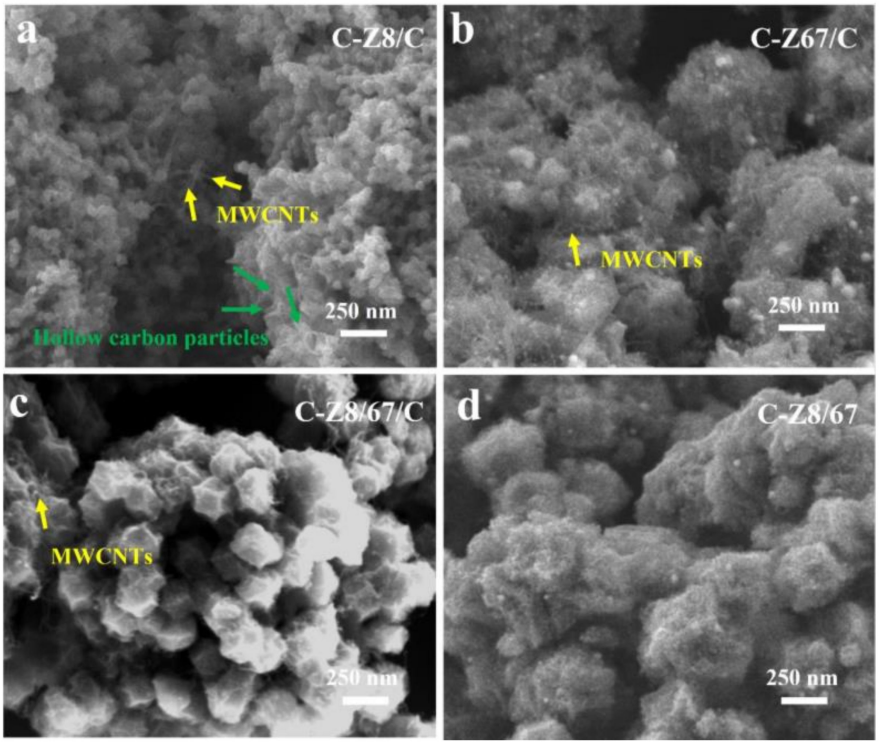

Figure 2. SEM images of (**a**) C-Z8/C, (**b**) C-Z67/C, (**c**) C-Z8/67/C, and (**d**) C-Z8/67.

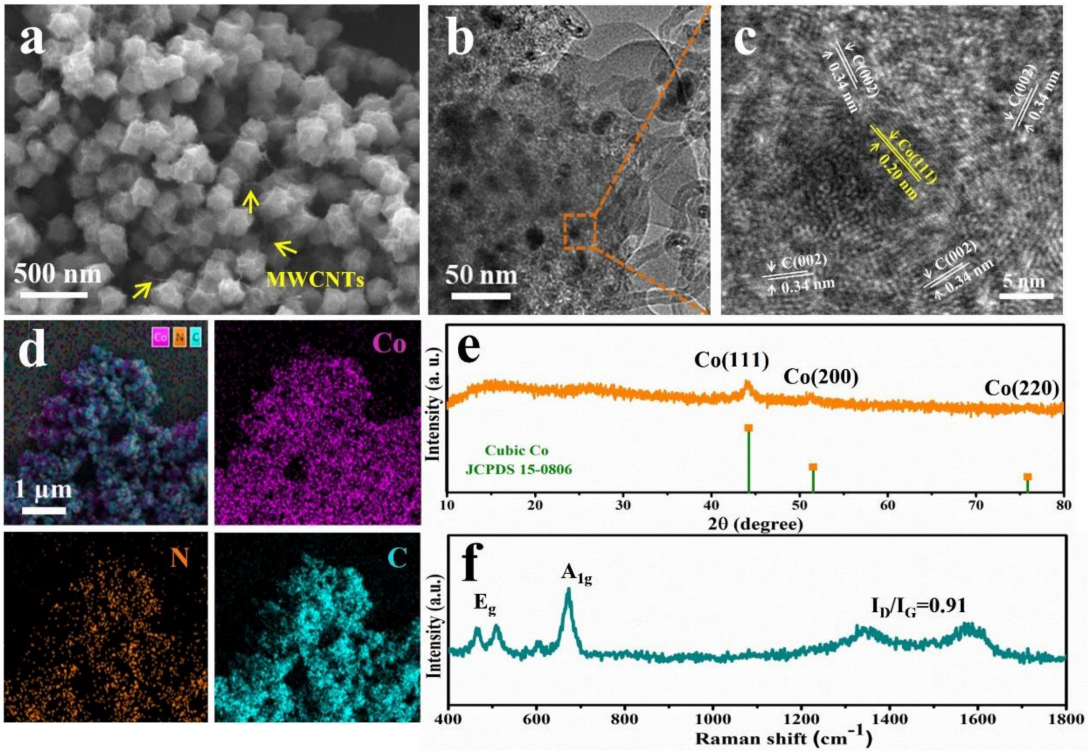

Figure 3. (**a**) SEM image (yellow arrows mean CNTs), (**b**) TEM figure, (**c**) High-resolution TEM figure with the indicator crystal plane of Co nanoparticles and graphitic carbon, (**d**) Element mappings of C, Co, N elements, (**e**) XRD pattern, and (**f**) Raman spectroscopy of the CNTs-Co@NCP.

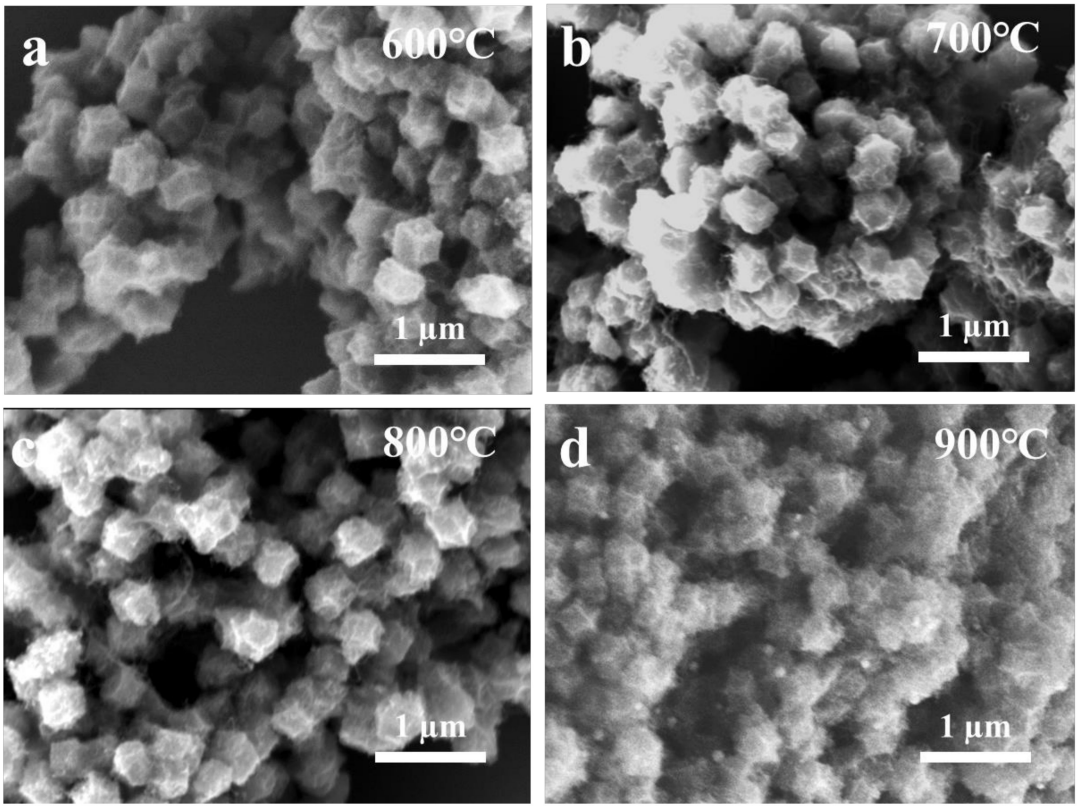

Figure 4. SEM images of C-Z8/67/C prepared at different pyrolysis temperatures: (**a**) 600 °C, (**b**) 700 °C, (**c**) 800 °C, and (**d**) 900 °C.

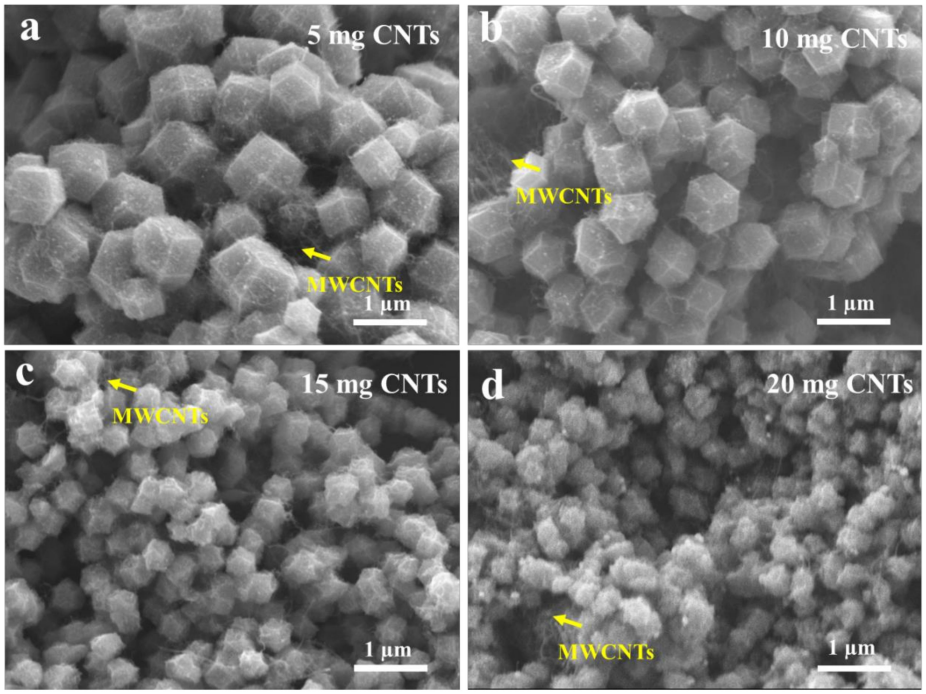

Figure 5. SEM images of C-Z8/67/C prepared with different mass of CNTs: (**a**) 5 mg, (**b**) 10 mg, (**c**) 15 mg, and (**d**) 20 mg.

The characterization results of the CNTs-Co@NCP are shown in Figure 3. TEM investigated a more detailed porous construction and graphitic level of the CNTs-Co@NCP, as shown in Figure 3b–c. The graphitic carbon transferred from amorphous carbon catalyzed by the inlaid Co nanoparticles [30]. From the elemental mapping analysis (Figure 3d), the Co, N, and C elements were evenly distributed throughout the CNTs-Co@NCP. Additionally, the species and structures in CNTs-Co@NCP were indicated via an X-ray diffraction pattern and Raman spectroscopy. As shown in Figure 3e, the peaks at 44.3°, 51.5°, and 75.9° correspond to the metallic Co (111), (200), and (220) planes. Figure 3f displays an obviously isolated D-band (~1351 cm^{-1}), which stands for the contribution of disorder or flaws, and G-band (~1582 cm^{-1}), which derives from the stretching of the C–C bonds in the graphitic construction. The degree of graphitization is evaluated, with an intensity proportion between the D-band and G-band (I_D/I_G). An I_G/I_D proportion of 0.91 for CNTs-Co@NCP means a graphitized construction, which may enhance the stability of the catalyst during electrochemical reactions.

N_2 adsorption/desorption measurement was made to reveal the porosity and the specific surface area (SSA) of samples, and Table 1 shows all the outcomes. It can be seen that the major influencing element of SSA is the bimetallic MOF precursor, but not the introduced CNTs [29]. Although the SSA of C-Z8/67/C is slightly less than that of C-Z8/67, the electrocatalytic activity of C-Z8/67/C is better than that of C-Z8/67, which is due to the exposed structure and the stereoconductive network of the C-Z8/67/C. Moreover, the tuning of CNTs mass also slightly affect the SSA. According to the Brunauer–Emmett–Teller measurement and pore distribution curves, the CNTs-Co@NCP construction holds a specific surface area (S_{BET}) of approximately 269.17 m^2 g^{-1} and a mean pore size of 4.27 nm (Figure 6a and inset, Table 1), implying mesopores in the composite framework. X-ray photoelectron spectroscopy was performed for the evaluation on the roles of different pyrolysis temperatures in the surface elementary constitute and chemical state of the catalyst. According to Figure 6b, the constituent elements of all the materials are C, N, Co, and O. CNTs-Co@NCP has the Co quantity of 12.23 wt%, more than that tested on the surface of CNTs-Co@NCP by XPS. The Co quantity tested via XPS surface exploration is underestimated. The sample prepared at 600 °C contains the highest O content, which

may be caused by residual cobalt-based precursor and incomplete carbonization. Figure 7 shows the deconvoluted Co 2p, N 1s, C 1s spectra of C-Z8/67/C. Binding energies around 780.5 and 796.3 eV conform to Co 2p3/2 and Co 2p1/2. Co 2p3/2 can be further deconvolved into Co^{3+} and Co^{2+} peaks at 780.21 and 782.62 eV, which are considered high-valence cobalt atoms (i.e., Co-N species) and effective active sites for ORR. Notably, the peak at 778.6 eV belongs to Co^0, indicating the presence of Co NPs. In high resolution XPS spectrum of N 1s, the peaks at 398.5, 400.1, 401.1, and 403.5 eV conform to pyridine-N, pyrrole-N, graphite-N, and O-N, while the peak located at 399.2 eV is Co-N_x. In case of a pyrolysis temperature of 800 °C, the high pyridine-N and Co-N_x quantity of C-Z8/67/C contributes to the competitive electrocatalysis (Figure 6c). Statistically the sum of the proportions of C-N and C=N in C-Z8/67/C-800 accounts for the largest one (Figure 6d), indicating that numerous C-N bonds generated during heat treatment. The C=N bonds facilitate electrons transfer and render more positive charges accumulated on Co atoms, which plays a positive role in improving eletrocatalytic activity. In Figure 6e, the total proportion of Co-N_x and CoC_xN_y in C-Z8/67/C-800 is dominant. It demonstrates that the Co-N_x and CoC_xN_y are the main catalytic activity contributors, which is consistent with the above conclusions. Figure 6f shows the atomic percentage of Co atoms in the samples created at various temperatures, and it is obvious that the proportion of Co atoms created at 800 °C is the highest, further indicating that the sample created at 800 °C has the highest density active site.

Table 1. Specific surface area and pore parameters of different samples.

Catalysts	SSA (m^2/g)	Pore Volume (cm^3/g)	Average Pore Size (nm)
C-Z8/C	212.90	0.28	4.60
C-Z67/C	203.31	0.21	4.01
C-Z8/67/C	275.09	0.39	5.22
C-Z8/67	280.72	0.30	4.08
C-Z8/67/C-600	189.73	0.18	3.89
C-Z8/67/C-700	242.34	0.23	3.76
C-Z8/67/C-800	270.80	0.32	4.40
C-Z8/67/C-900	275.09	0.39	5.22
C-Z8/67/C-5	259.12	0.25	3.69
C-Z8/67/C-10	263.96	0.29	4.24
C-Z8/67/C-15	269.17	0.31	4.27
C-Z8/67/C-20	270.80	0.32	4.40

2.2. Electrocatalytic Activity

To systematically evaluate the effects of different composition, pyrolysis temperature, and CNTs mass on electrocatalytic activity, rotating disk/rotating ring-disk electrode (RDE/RRDE) measurements were performed in 0.1 M KOH electrolyte. It has been proven that bimetallic MOF coupled with introduced CNTs is a useful method to improve ORR electrocatalytic activity. The cyclic voltammetry (CV) and linear sweep voltammetry (LSV) polarization curves of the materials under different synthesis conditions are shown in Figure 8, and the $E_{1/2}$ and J_L of all samples are listed in Table 2. According to the difference in composition, it can be considered that the active site of C-Z8/C is C-N_x, while the active sites of Co-based catalysts are Co-N_x and C-N_x. MWCNTs and C-Z8/C basically exhibit low ORR electrocatalytic activity, while C-Z67/C, C-Z8/67, and C-Z8/67/C catalysts show relatively higher catalytic activity. It demonstrates that the introduction of ZIF-67 precursor can significantly improve electrocatalytic activity. The enhanced diffusion-limited current density is caused by the unique structural design. On this basis, the influence of pyrolysis temperature on electrocatalytic activity was examined. Figure 8a,b shows the CV and LSV polarization curves of the materials under different pyrolysis temperatures. In alkaline medium, C-Z8/67/C-600 and C-Z8/67/C-700 show poor ORR electrocatalytic activity because of the incomplete carbonization and low electrical conductivity. There are both significant differences of $E_{1/2}$ and J_L between samples C-Z8/67/C-700 and C-Z8/67/C-

800. Additionally, there are no significant differences in $E_{1/2}$ but a clear difference in J_L between the samples C-Z8/67/C-800 and C-Z8/67/C-900. In short, the optimal pyrolysis temperature is 800 °C. Considering the influence of introducing different mass of CNTs on the structure of hybrids, further testing experiments are carried out to validate the effect on electrocatalytic activity. It was found that too many or too few CNTs are not conducive to performance. As shown in Figure 8c,d, the $E_{1/2}$ of CNTs-Co@NCP is 0.86 V at a rotation speed of 1600 rpm in 0.1 M KOH electrolyte, and the J_L reaches 5.94 mA/cm^2. The largest J_L of the CNTs-Co@NCP reveals that it has an appropriate surface area and mass transfer. The ORR kinetics of all the samples above were compared by Tafel slope. For catalysts C-Z8/C, C-Z67/C, C-Z8/67, and C-Z8/67/C, the Tafel slopes (Table 2) are 97 mV/dec, 60 mV/dec, 78 mV/dec, and 59 mV/dec. C-Z8/67/C has slightly less Tafel slope than commercial Pt/C (62 mV/dec), indicating that the co-existence of Co-based carbonaceous materials and CNTs promotes ORR kinetics, and the one-dimensional CNT structure effectively enhances electron transport capacity. The global conductive network and open microstructure brought by the 1D/3D coupling structure construction are the most important factors of high electrocatalytic activity. The Tafel slopes of the C-Z8/67/C-600, C-Z8/67/C-700, C-Z8/67/C-800, and C-Z8/67/C-900 are 68 mV/dec, 63 mV/dec, 53 mV/dec, and 60 mV/dec. The effect of pyrolysis temperature on kinetic performance is not too different. The Tafel slopes of the C-Z8/67/M-5, C-Z8/67/M-10, CNTs-Co@NCP, and C-Z8/67/M-20 are 60 mV/dec, 58 mV/dec, 54 mV/dec, and 59 mV/dec. The CNTs-Co@NCP sample has an optimal kinetic performance. The introduced CNTs can enhance the kinetic performance of the catalyst. The regulation of carbonization temperature and CNTs mass mainly contributes to the optimization of carbonaceous framework and the performance improvement of the catalyst, but the contribution to catalyst activity is the composition tuning. In conclusion, the high catalytic activity of CNTs-Co@NCP is the result of synergy of composition and structure.

Table 2. The $E_{1/2}$, J_L, and Tafel slopes of different samples.

Catalysts	$E_{1/2}$ (V)	J_L (mA/cm^2)	Tafel Slope (mV/dec)
C-Z8/C	0.698	3.765	97
C-Z67/C	0.804	4.965	60
C-Z8/67/C	0.836	5.343	59
C-Z8/67	0.840	4.894	78
C-Z8/67/C-600	0.794	4.613	68
C-Z8/67/C-700	0.812	4.502	63
C-Z8/67/C-800	0.845	5.315	53
C-Z8/67/C-900	0.834	4.824	60
C-Z8/67/C-5	0.850	4.991	60
C-Z8/67/C-10	0.856	5.194	58
C-Z8/67/C-15 (CNTs-Co@NCP)	0.860	5.940	54
C-Z8/67/C-20	0.851	5.706	59

For more knowledge about the great ORR electrocatalytic activity of CNTs-Co@NCP, the enumeration of LSVs of CNTs-Co@NCP on RDE with different rotating rates was implemented within Figure 9a. The gradual enhancement of the limited diffusion current density of a catalyst is realized as the rotation speed increases, and the calculation of electron transfer number (n) can be calculated using the Koutecky–Levich (K–L) equation. According to Figure 9b, the linear association between the inverse current and the inverse of the square root of rotation speed. n for the CNTs-Co@NCP reached the value of 3.9 at 0.3–0.7 V from the K–L plot slope, showing a near-complete decrease process of oxygen into water and indicating a predominant four-electron reduction pathway toward ORR. LSV curves of CNTs-Co@NCP and Pt/C were examined within an O_2-saturated 0.1 M KOH solution with the rotating and scan rates of 1600 rpm and 10 mV s^{-1} according to Figure 9c. The Pt/C shows an $E_{1/2}$ of 0.86 V versus RHE and a diffusion-limited current density of

~6.0 mA cm^{-2}. The performance of CNTs-Co@NCP is comparable to Pt/C. It indicates that the 1D/3D mesoporous structure makes contributions to the improvement of mass transfer and exposed surface. In addition to RDE measurements, RRDE measurements were made to supervise ORR routes and assess ORR kinetics (Figure 9d). In the case of a rotation speed of 1600 rpm, the disk current is much greater than the loop current. The yield of H_2O_2 shown by RRDE information was less than 7.5% on CNTs-Co@NCP in the hidden scope of 0.3–0.8 V. CNTs-Co@NCP has an obvious four-electron decrease process. The above outcomes show that CNTs-Co@NCP has been a hidden non-noble metal catalyst. The comparison of the performance of different ZIF-8/67-derived catalysts for electrocatalytic ORR are listed in Table 3.

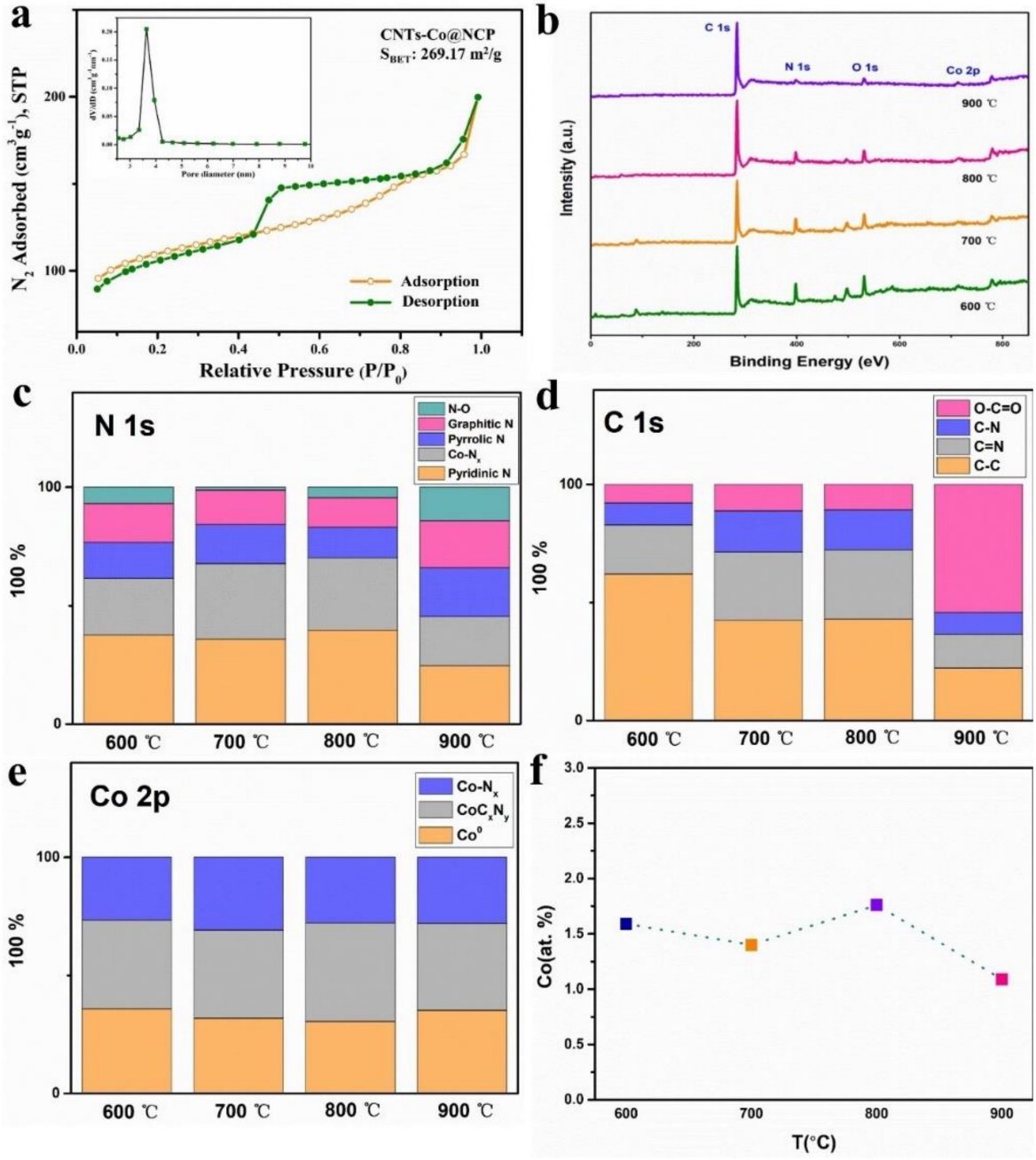

Figure 6. (**a**) BET and the pore-size distribution curve of the CNTs-Co@NCP. (**b**) XPS survey spectrum of C-Z8/67/C prepared at different pyrolysis temperatures. Percentages of different components of deconvoluted (**c**) N 1s, (**d**) Co 2p, and (**e**) C 1s high-resolution XPS spectroscopy. (**f**) Co atom percentage in the catalysts.

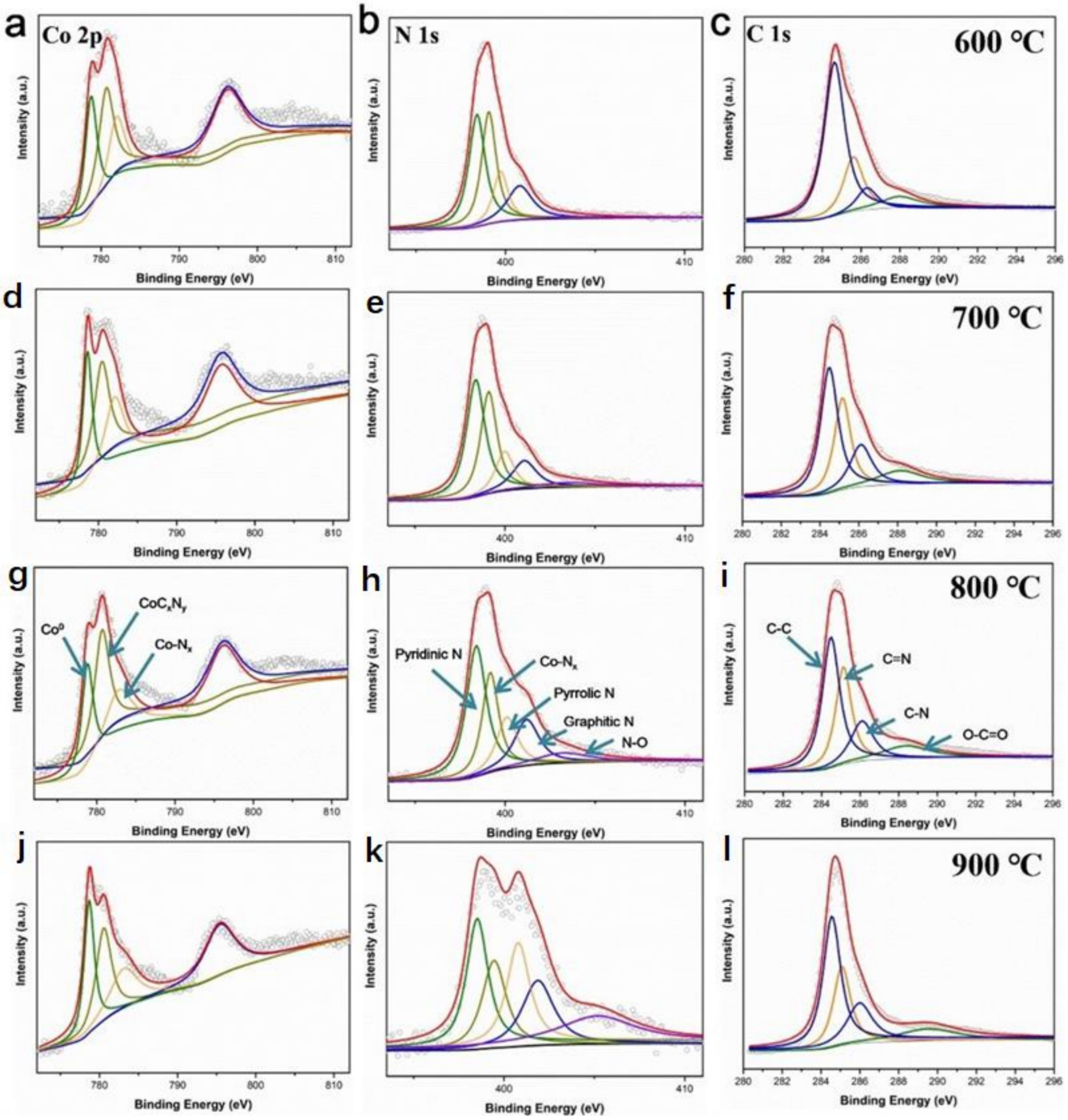

Figure 7. The experimental and fitted high-resolution XPS spectra of Co 2p, N 1s, and C 1s for C-Z8/67/C prepared at different pyrolysis temperatures: (**a**–**c**) 600 °C, (**d**–**f**) 700 °C, (**g**–**i**) 800 °C, and (**j**–**l**) 900 °C.

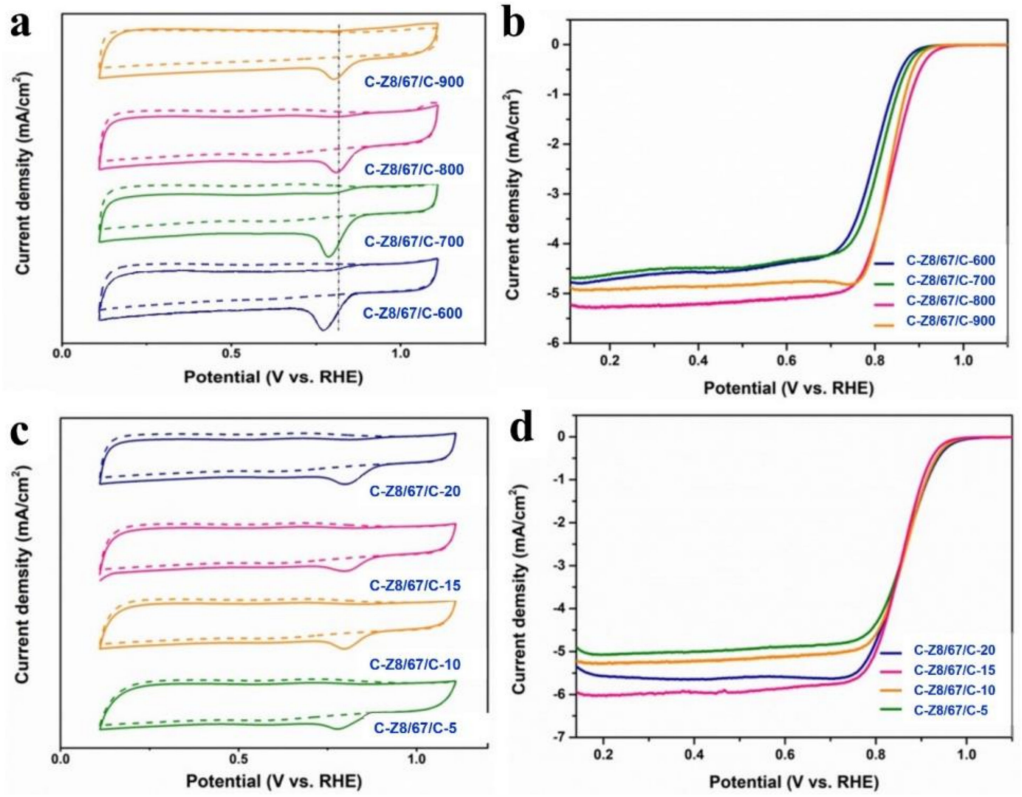

Figure 8. (**a**,**c**) CV and (**b**,**d**) LSV polarization curves of the materials under different synthesis.

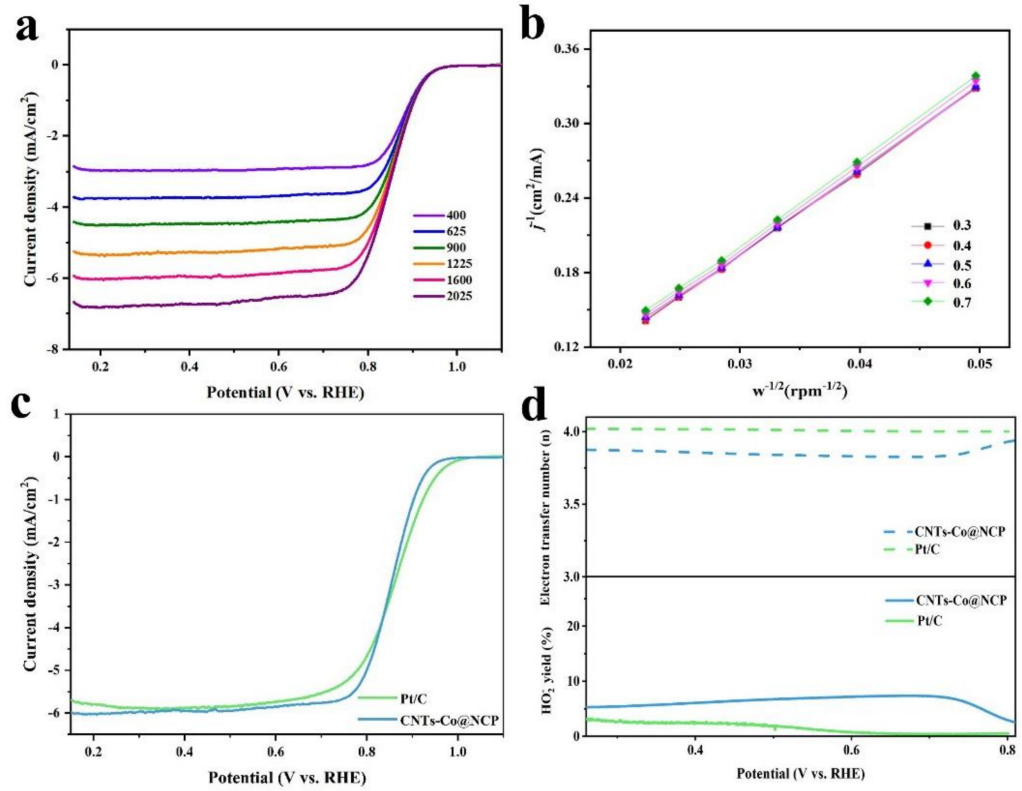

Figure 9. (**a**) LSVs and (**b**) calculated K–L plots with varied potentials of CNTs-Co@NCP. (**c**) LSV and (**d**) Peroxide yields (H_2O_2%) and electron transfer numbers of CNTs-Co@NCP and Pt/C.

Table 3. Performance comparison for different ZIF-8/67-derived catalysts for electrocatalytic ORR.

Sample	$E_{1/2}$ (V)	J_L (mA/cm^2)	Electrolyte	Ref.
CNTs-Co@NCP	0.86	5.94	0.1 M KOH	This work
NAC@Co_3O_4/NCNTs/CNF	0.83	5.6	0.1 M KOH	[4]
NC@CC	0.89	~4.4	0.1 M KOH	[5]
Core-shell Co,N-HCNP	0.855	5.0	0.1 M KOH	[6]
GO/ZIF-8@ZIF-67-900	~0.82	5.1	0.1 M KOH	[7]
FCNC900	0.868	-	0.1 M KOH	[8]
Co/Co_4N@N-CNTs/rGO	~0.83	4.82	0.1 M KOH	[9]
Zn/Co-NC	0.856	~5.6	0.1 M KOH	[10]
Co-NSC 200	0.74	5.53	0.1 M $HClO_4$	[11]
ZnCoFe-N-C	0.878	~5.0	0.1 M KOH	[12]
Co@N-CNT-HC	0.84	4.7	0.1 M KOH	[13]
CoNHPC-920	0.87	5.41	0.1 M KOH	[14]
ES-CNCo-5	–0.155 vs. Ag/AgCl	4.82	0.1 M KOH	[15]
CoFeZn@pCNT	0.87	~5.2	0.1 M KOH	[16]
Co,N-C/TOCNF	0.74 V vs. SHE	4.5	0.1 M KOH	[17]
BM_2-C_6-50^T	0.84	5.26	0.1 M KOH	[18]
CNT@SAC-Co/NCP	0.870	~5.25	0.1 M KOH	[19]
CoZnNC-2	0.85	5.41	0.1 M KOH	[20]
Co SA/NCFs	0.85	~6.0	0.1 M KOH	[21]
Co-N-RGO	0.75	5.25	0.5 M H_2SO_4	[22]
Co-N/S-C-3.5	0.80	4.2	0.1 M KOH	[23]
Co_9S_8/NSC	0.82	~5.4	0.1 M KOH	[24]
$ZnCo_2$@NCNTs-800	0.85	~6.2	0.1 M KOH	[25]
$FeZn_4Co$@CNFs	0.84	~4.95	0.1 M KOH	[26]
Co_3O_4/CNTs	0.86	5.65	0.1 M KOH	[27]

2.3. Stability and Methanol Tolerance

Aside from the enhanced catalytic activity, CNTs-Co@NCP also demonstrated excellent stability under potentiostatic conditions. After 5000 CV cycles (Figure 10a,b), the $E_{1/2}$ of CNTs-Co@NCP was almost unaltered, which suggested excellent steadiness under hidden cycling. Correspondingly, the $E_{1/2}$ value of Pt/C in Figure 10c varies greatly. Within O_2-saturated 0.1 M KOH solution, the measurement of chronoamperometry (*i-t*) curves of CNTs-Co@NCP and Pt/C was made with 0.7 V at the rotation of 1600 rpm. According to Figure 11a, the CNTs-Co@NCP catalyst kept up to 88% of its first current density, showing improved high stability and durability relative to the Pt/C inspected. To show the property of great ORR steadiness, the CNTs-Co@NCP catalyst after ORR steadiness inspection was characterized by XPS (Figure 11b). By comparing with initial CNTs-Co@NCP, the unchanged Co 2p peak shapes and binding energies can be seen. The strengthened steadiness possibly benefited from the inherently steady 1D/3D interwoven structure.

The CV inspections within O_2-saturated 1.0 M KOH solution with or without methanol (1.0 M) were made to investigate the CNTs-Co@NCP and Pt/C methanol tolerance property according to Figure 11d and e. Nearly no variation is found in the oxygen reduction peak of CNTs-Co@NCP, indicating CNTs-Co@NCP has excellent tolerance for methanol crossover. Contrarily, the CV curve of Pt/C displays a great methanol oxidation peak, showing the poor methanol tolerance of Pt/C. Additionally, the *i-t* technique was adopted to assess and compare methanol tolerance of CNTs-Co@NCP and commercial Pt/C (Figure 11f). After injecting methanol at 900 s, there is no great change in ORR current density of the CNTs-Co@NCP, indicating a great resistance to methanol cross-effects. Oppositely, the Pt/C catalyst displays a great decline within ORR current density because of the intrinsic vulnerability to methanol of Pt.

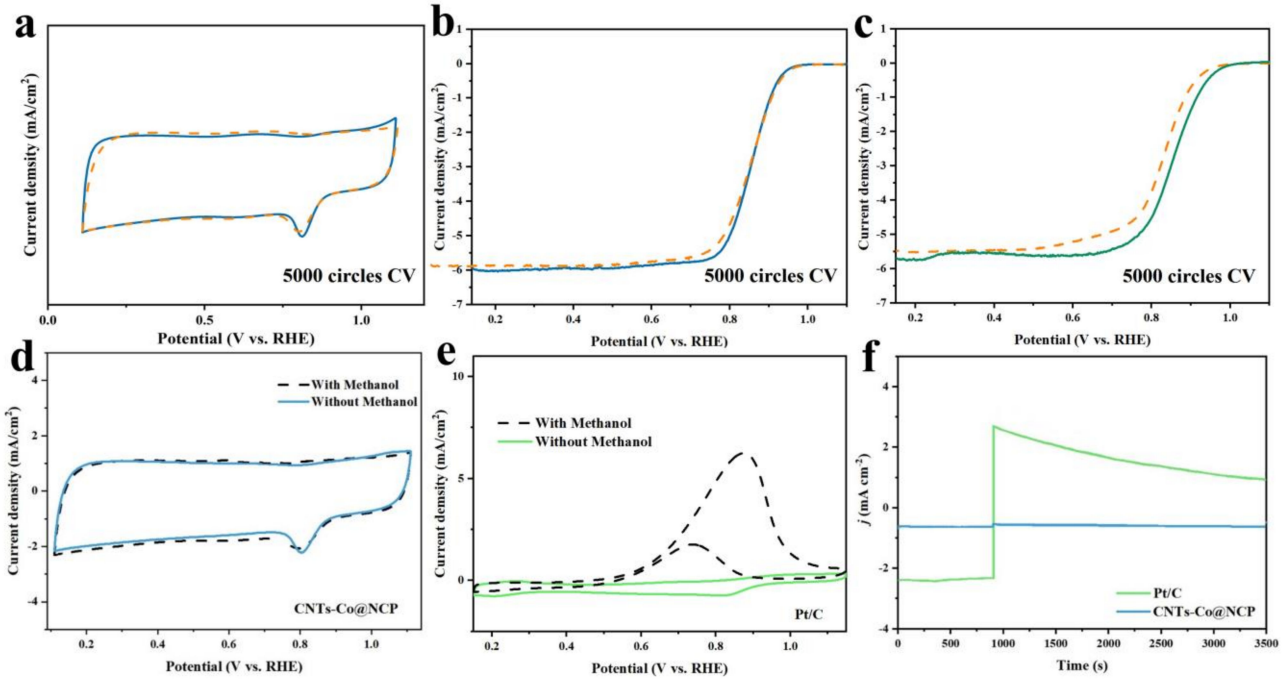

Figure 10. (**a**) Before and after 5000 cycles, CV and (**b**) LSV curves of CNTs-Co@NCP. (**c**) Before and after 5000 cycles, LSV of Pt/C. CV curves of (**d**) CNTs-Co@NCP and (**e**) Pt/C with and without 1.0 M methanol in 0.1 M KOH. (**f**) Chronoamperometric reactions for the comparison of CNTs-Co@NCP and Pt/C with or without methanol.

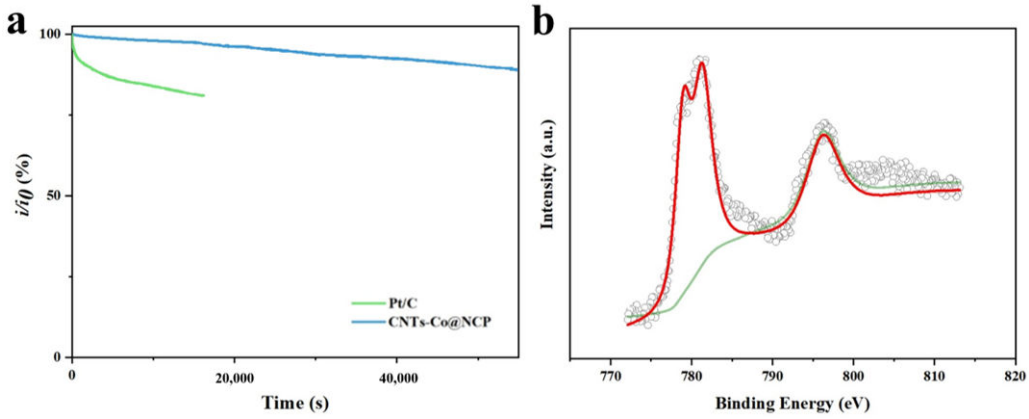

Figure 11. (**a**) Chronoamperometric responses within CNTs-Co@NCP and Pt/C catalysts. (**b**) XPS of Co 2p after ORR stability test.

2.4. Fuel Cells Tests

Inspired by the enhanced ORR electrocatalytic activity and the intrinsic steadiness and methanol tolerance of CNTs-Co@NCP catalyst, an DMFC was assembled with CNTs-Co@NCP as the cathode catalyst and further used to assess the practical usage in energy-conversion equipment. Figure 12 presents the polarization curves of DMFCs adopting both the CNTs-Co@NCP and commercial Pt/C at the cathode of a membrane electrode assembly (MEA). The evaluation of the performance of 4.5 mg cm^{-2} CNTs-Co@NCP loading for the cathodic electrode was evaluated at 60 °C for portable usage (Figure 12a). The application of a high methanol concentration at the anode is advantageous; oppositely, the major defect is the methanol crossover by the anionic exchange membrane. Here, the increase in methanol concentration does not influence cell performance obviously because of the excellent methanol tolerance of CNTs-Co@NCP electrocatalysts (Figure 12b). As the methanol concentration increases from 1.0 M to 5.0 M, the DMFC shows steady

power density and current density. Particularly, the highest power density (46.6 mW cm^{-2}) and current density (94.5 mA cm^{-2}) were obtained with 3.0 M methanol at the anode. Figure 12c compares open circuit voltages (OCV) under various methanol concentrations. The MEA, adopting the CNTs-Co@NCP catalyst, realized an OCV of 0.93 V at 1.0 M methanol at the anode. Oppositely, the OCV of the MEA applying the Pt/C cathode was only 0.82 V, indicating a voltage loss. Additionally, as the methanol concentration increased, the Pt/C cathode showed a constant and quick decline in OCVs and a great regression of peak power density (Figure 12d). Additionally, the deterioration in the mass transfer region is greatly relieved with the CNTs-Co@NCP cathode, confirming that the best CNTs-Co@NCP catalyst has beneficial porosity and morphology for enhanced mass transport. The excellent performance may be caused by various elements, such as the strengthened inherent ORR activity of the uniformly dispersed active sites, excellent methanol tolerance, and the enhanced mass move from beneficial mesopores in the catalysts. Hence, the CNTs-Co@NCP catalyst would potentially be viable to use in DMFCs with enhanced performance and durability.

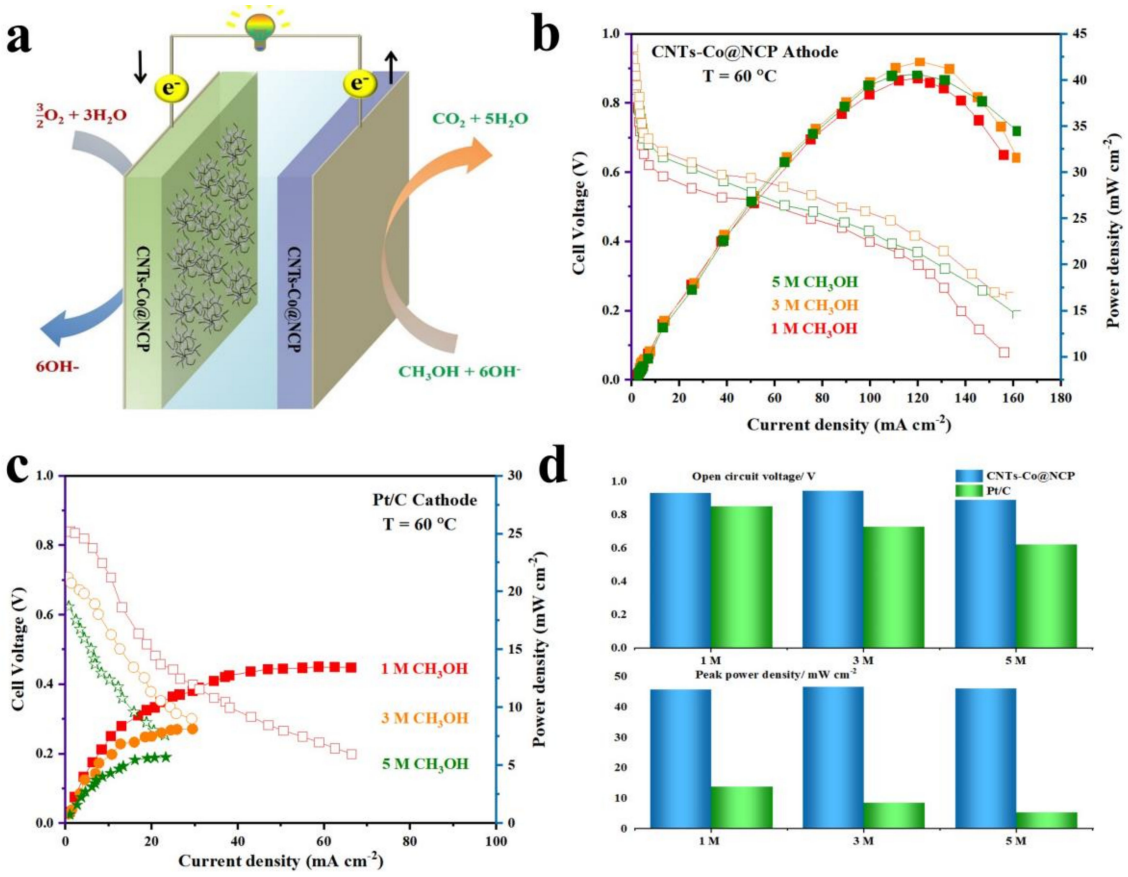

Figure 12. (**a**) Schematic diagram of a DFMC. Polarization plots of the cell voltage and power density versus current density of the DMFC with (**b**) CNTs-Co@NCP and (**c**) Pt/C as cathode catalysts. (**d**) OCV and peak power density of the CNTs-Co@NCP and Pt/C catalysts adopted in the DMFC. Anode: 4.0 mg cm^{-2} PtRu/C; cathode: 4.5 mg cm^{-2} CNTs-Co@NCP or 0.9 mg cm^{-2} Pt/C; methanol flow rate of 0.5 mL min^{-1}; membrane: FAA-3-50; cell: 60 °C.

3. Experimental Section

3.1. Chemicals and Materials

All reagents, $Zn(NO_3)_2 \cdot 6H_2O$ (99% purity), $Co(NO_3)_2 \cdot 6H_2O$ (99% purity), 2-methylimidazole (≥98% purity), methanol (99.5% purity), MWCNTs, and Nafion® 5 wt.% hydroalcoholic solutions were obtained from commercial suppliers (Aladdin Biological Technology Co.,

Ltd., Shanghai, China), and used without further purification unless otherwise noted. Mili-Q water has been applied in all experiments.

3.2. Synthesis of CNTs-Co@NCP

$Zn(NO_3)_2{\cdot}6H_2O$ and $Co(NO_3)_2{\cdot}6H_2O$ were dissolved within 50 mL of methanol solution. Later, different masses of MWCNTs were dispersed in the above solution and sonicated to homogeneity. Then, 50 mL methanol solution containing 2-methylimidazole was quickly added into the mixed system. Last, the as-synthesized ZIF-8/67/CNTs were annealed at different temperatures.

3.3. Electrochemical Measurements

All electrochemical measurements have been conducted within the CHI 760E electrochemical workstation (CH Instruments Inc., Shanghai, China) at room temperature, using the thin-film rotating disk electrode (RDE) and rotating ring-disk electrode (RRDE) within the custom three-electrode system, which consisted of the counter electrode (graphite carbon), reference electrode (saturated calomel electrode, SCE), as well as the modified working electrode (glassy carbon, diameter: 5 mm). Both RDE and RRDE systems were employed to investigate the ORR catalytic activity of as-prepared materials in an oxygen-saturated 0.1 M KOH electrolyte. The electrode potential was called reversible hydrogen electrode (RHE). The current density was normalized to the glass-like carbon disk electrode. The catalyst loading was 0.255 mg cm^{-2}.

3.4. Characterizations

Morphology, crystal phase and composition of as-prepared samples have been passed through a scanning electron microscope (SEM, 3 kV, Hitachi S4800, Hitachi, Tokyo, Japan) equipped with an energy-dispersive spectrometer (EDS), transmission electron microscopy (TEM, at 200 kV, JEM-2011-HR, JEOL, Tokyo, Japan), and X-ray diffraction (XRD, D/max2550VB3+/PC, Rigaku Inc., Tokyo, Japan) with Cu Kα radiation (λ = 0.15418 nm). An X-ray photoelectron spectroscopy (XPS) PHI-5000C ESCA system (PerkinElmer, Waltham, MA, USA) with Mg Kα radiation together with C 1s peak at 284.6 eV to be internal standard has been adopted to analyze the surface elemental composition of the powder. Raman spectra have been carried upon the Laser Raman spectrometer (in Via, Renishaw, Pliezhausen, Germany) with the 514 nm laser. The surface area has been measured in both N_2 adsorption and desorption isotherm via the Brunauer–Emmett–Teller (BET) method. Pore size distribution was retrieved by applying the Barrett–Joyner–Halanda (BJH) method in an adsorption branch of isotherm.

3.5. Evaluation of the Electron-Transfer rate, Mass and Specific Activities

The working electrode was scanned at a sweep rate of 10 mVs^{-1} using various rotation rates (w): 400, 625, 900, 1225, 1600, and 2025 rpm.

Kouteky–Levich (K–L) curve analysis was applied to calculate the number of electrodes transferred (n) according to the K–L equation as follows:

$$\frac{1}{i} = \frac{1}{i_k} + \left(\frac{1}{0.62nFAD^{2/3}v^{-1/6}C^0}\right)\omega^{-1/2} \quad (1)$$

where i is the measured current and i_k is the kinetic current. F, A, D, v, C^0, n and ω are the Faraday constant, the electrode geometry area, the diffusion coefficient of oxygen, the kinematic viscosity, the concentration of oxygen in the 0.1 M KOH electrolyte, the number of electrons transferred, and the rotation rate for electrode, respectively.

3.6. Rotating Ring-Disk Electrode (RRDE)

In the RRDE measurements, the linear sweep voltammograms (LSVs) were recorded in O_2 saturated 0.1 M KOH electrolyte with a scan rate of 10 mV s^{-1} at a rotating speed of 1600 rpm.

During the test, the ring potential was fixed at 1.2 V versus RHE. The ORR current was rectified using the background current. The hydrogen peroxide yield (H_2O_2%) and total number of electron-transfer number (n) in the ORR were evaluated as follows:

$$H_2O_2\% = 200 \times (i_r/N)/[i_d + (i_r/N)] \quad (2)$$

$$N = 4 \times i_d/[i_d + (i_r/N)] \quad (3)$$

where i_d and i_r are the disk and ring currents, respectively. N is the RRDE current collection efficiency determined to be 0.37 by the reduction of 10 mM $K_3[Fe(CN)_6]$ in 0.1 M KNO_3.

4. Conclusions

In brief, N-containing carbon-based catalyst CNTs-Co@NCP was successfully prepared from bimetallic MOF coupled with specially introduced CNTs. The electrocatalytic performance of catalysts under different synthetic conditions, including different compositions, pyrolysis temperature, and introduced CNTs mass, was fully investigated. We found that, in addition to the composition and pyrolysis temperature, the mass of introduced CNTs played a positive role in the improvement of electrocatalytic results. The prepared CNTs-Co@NCP generated an excellent ORR activity and selectivity to the 4e pathway under basic conditions. When the CNTs-Co@NCP was assembled into a DMFC, the most power density (46.6 mW cm^{-2}) was obtained with 3.0 M methanol at the anode. The CNTs-Co@NCP catalyst has great potential for viable usage in DMFCs with enhanced performance and durability. It should be noted that the electrocatalytic property of CNTs-Co@NCP under acidic conditions was not studied in this work, and the stability of the catalyst in DMFC work also needs further investigation. The incomplete work will be improved in future work.

Author Contributions: Y.Z. and Y.T.: Conceptualization, Methodology, Investigation, Data curation, Formal analysis, Writing—original draft, Writing—review and editing. H.S., S.L. and P.T.: Writing—review and editing. All authors have read and agreed to the published version of the manuscript.

Funding: This research received no external funding.

Data Availability Statement: Not applicable.

Conflicts of Interest: The authors declare no conflict of interest.

References

1. Shi, H.; Peng, J.; Cheng, X.; Yang, X.; Jin, J.; Hu, J. The CO_2 desorption analysis of tri-solvent MEA + BEA + DEEA with several commercial solid acid catalysts. *Int. J. Greenh. Gas Control.* **2022**, *116*, 103647. [CrossRef]
2. Wang, Z.; Huang, J.; Wang, L.; Liu, Y.; Liu, W.; Zhao, S.; Liu, Z. Cation-Tuning Induced d-Band Center Modulation on Co-Based Spinel Oxide for Oxygen Reduction/Evolution Reaction. *Angew. Chem. Int. Ed.* **2022**, *61*, e202114696. [CrossRef] [PubMed]
3. Wang, C.; Ha, Y.; Mao, X.; Xu, W.; Du, A.; Wu, R.; Chou, S.; Zhang, H. Co Nanoparticles Encapsulated in N-Doped Carbon Nanotubes Grafted CNTs as Electrocatalysts for Enhanced Oxygen Reduction Reaction. *Adv. Mater. Interfaces* **2022**, *9*, 2101877. [CrossRef]
4. Yao, X.; Wang, X.; Sun, L.; Li, L.; Kan, E.; Ouyang, B.; Zhang, W. Popcorn-like Co_3O_4 nanoparticles confined in a three-dimensional hierarchical N-doped carbon nanotube network as a highly-efficient trifunctional electrocatalyst for zinc–air batteries and water splitting devices. *Inorg. Chem. Front.* **2022**, *9*, 2517–2529. [CrossRef]
5. Wang, Z.; Lu, Y.; Yan, Y.; Larissa, T.Y.P.; Zhang, X.; Wuu, D.; Zhang, H.; Yang, Y.; Wang, X. Core-shell carbon materials derived from metal-organic frameworks as an efficient oxygen bifunctional electrocatalyst. *Nano Energy* **2016**, *30*, 368–378. [CrossRef]
6. Hu, Z.; Zhang, Z.; Li, Z.; Dou, M.; Wang, F. One-Step Conversion from Core-Shell Metal-Organic Framework Materials to Cobalt and Nitrogen Codoped Carbon Nanopolyhedra with Hierarchically Porous Structure for Highly Efficient Oxygen Reduction. *ACS Appl. Mater. Interfaces* **2017**, *9*, 16109–16116. [CrossRef]
7. Wei, J.; Hu, Y.; Liang, Y.; Kong, B.; Zheng, Z.; Zhang, J.; Jiang, S.P.; Zhao, Y.; Wang, H. Graphene oxide/core-shell structured metal-organic framework nano-sandwiches and their derived cobalt/N-doped carbon nanosheets for oxygen reduction reactions. *J. Mater. Chem. A* **2017**, *5*, 10182–10189. [CrossRef]
8. Jose, V.; Jayakumar, A.; Lee, J. Bimetal/Metal Oxide Encapsulated in Graphitic Nitrogen Doped Mesoporous Carbon Networks for Enhanced Oxygen Electrocatalysis. *ChemElectroChem* **2018**, *6*, 1485–1491. [CrossRef]

9. Qi, H.; Feng, Y.; Chi, Z.; Cui, Y.; Wang, M.; Liu, J.; Guo, Z.; Wang, L.; Feng, S. *In situ* encapsulation of Co-based nanoparticles into nitrogen-doped carbon nanotubes-modified reduced graphene oxide as an air cathode for high-performance Zn–air batteries. *Nanoscale* **2019**, *11*, 21943–21952. [CrossRef]
10. Fang, F.; Wu, Z.; Zheng, D.; Guo, M.; Li, X.; Li, Z.; Wei, Y.; Liu, X.; Tong, Y.; Dong, X.; et al. ZnO@zeolitic imidazolate frameworks derived porous hybrid hollow carbon shell as an efficient electrocatalyst for oxygen reduction. *J. Mater. Sci.* **2021**, *56*, 14989–15003. [CrossRef]
11. Lee, J.S.; Rajan, H.; Christy, M.; Yi, S.C. Optimization of active sites by sulfurization of the core–shell ZIF 67@ZIF 8 for rapid oxygen reduction kinetics in acidic media. *Int. J. Hydrogen Energy* **2021**, *46*, 10739–10748. [CrossRef]
12. Li, G.; Deng, W.; He, L.; Wu, J.; Liu, J.; Wu, T.; Wang, Y.; Wang, X. Zn, Co, and Fe Tridoped N-C Core-Shell Nanocages as the High-Efficiency Oxygen Reduction Reaction Electrocatalyst in Zinc-Air Batteries. *ACS Appl. Mater. Interfaces* **2021**, *13*, 28324–28333. [CrossRef] [PubMed]
13. Li, K.; Zhang, Y.; Wang, P.; Long, X.; Zheng, L.; Liu, G.; He, X.; Qiu, J. Core-Shell ZIF-67@ZIF-8-derived multi-dimensional cobalt-nitrogen doped hierarchical carbon nanomaterial for efficient oxygen reduction reaction. *J. Alloy. Compd.* **2022**, *903*, 163701. [CrossRef]
14. Zhang, Y.; Yang, M.; Wang, P.; Li, K.; Li, S.; Zhang, Z.; He, X.; Duan, Y. Co/N-codoped carbon nanotube hollow polyhedron hybrid derived from salt-encapsulated core-shell ZIF-8@ZIF-67 for efficient oxygen reduction reaction. *J. Alloy. Compd.* **2022**, *904*, 164083. [CrossRef]
15. Zhang, C.-L.; Lu, B.-R.; Cao, F.-H.; Wu, Z.-Y.; Zhang, W.; Cong, H.-P.; Yu, S.-H. Electrospun metal-organic framework nanoparticle fibers and their derived electrocatalysts for oxygen reduction reaction. *Nano Energy* **2018**, *55*, 226–233. [CrossRef]
16. Agarwal, S.; Yu, X.; Manthiram, A. A pair of metal organic framework (MOF)-derived oxygen reduction reaction (ORR) and oxygen evolution reaction (OER) catalysts for zinc-air batteries. *Mater. Today Energy* **2020**, *16*, 100405. [CrossRef]
17. Lee, Y.-R.; Yoo, H.; Choi, J.; Ahn, W.-S. Electrocatalytic oxygen reduction over Co@Co_3O_4/N-doped porous carbon derived from pyrolysis of ZIF-8/67 on cellulose nanofibers. *Cellulose.* **2020**, *27*, 2723–2735. [CrossRef]
18. Li, C.; Li, Y.; Yao, Z.; Wang, J.; Zhong, Q. A mild approach to bimetallic ZIF-derived porous carbons as highly efficient oxygen reduction electrocatalysts. *Int. J. Hydrogen Energy* **2021**, *46*, 6188–6196. [CrossRef]
19. Li, J.; Meng, Y.; Zhang, L.; Li, G.; Shi, Z.; Hou, P.; Liu, C.; Cheng, H.; Shao, M. Dual-Phasic Carbon with Co Single Atoms and Nanoparticles as a Bifunctional Oxygen Electrocatalyst for Rechargeable Zn-Air Batteries. *Adv. Funct. Mater.* **2021**, *31*, 2103360. [CrossRef]
20. Chen, D.; Huang, Q.; Ding, J.; Li, T.-T.; Yu, D.; Nie, H.; Qian, J.; Yang, Z. Heteroepitaxial metal-organic frameworks derived cobalt and nitrogen codoped carbon nanosheets to boost oxygen reduction. *J. Colloid Interface Sci.* **2022**, *623*, 1210–1219. [CrossRef]
21. Han, Y.; Duan, H.; Zhou, C.; Meng, H.; Jiang, Q.; Wang, B.; Yan, W.; Zhang, R. Stabilizing Cobalt Single Atoms via Flexible Carbon Membranes as Bifunctional Electrocatalysts for Binder-Free Zinc-Air Batteries. *Nano Lett.* **2022**, *22*, 2497–2505. [CrossRef]
22. Lian, J.; Bai, Q.; Zhao, J.; Wang, X. Highly dispersed Co-N-RGO electrocatalyst based on an interconnected hierarchical pore framework for proton exchange membrane fuel cells. *Catal. Sci. Technol.* **2022**, *12*, 6285–6293. [CrossRef]
23. Liu, Z.; Wang, D.; Kou, X.; Dong, X.; Chi, X.; Ma, H.; Wang, G. High-performance oxygen reduction electrocatalysts derived from bimetal-organic framework and sulfur-doped precursors for use in microbial fuel cells. *J. Power Sources* **2021**, *521*, 230944. [CrossRef]
24. Peng, Y.; Zhang, F.; Zhang, Y.; Luo, X.; Chen, L.; Shi, Y. N,S-Doped hollow carbon nanosheet-encapsulated Co_9S_8 nanoparticles as a highly efficient bifunctional electrocatalyst for rechargeable zinc–air batteries. *Dalton Trans.* **2022**, *51*, 12630–12640. [CrossRef] [PubMed]
25. Qin, T.; Li, F.; Liu, X.; Yuan, J.; Jiang, R.; Sun, Y.; Zheng, H.; O'Mullane, A.P. Template-Assisted Synthesis of High-Efficiency Bifunctional Catalysts with Roller-Comb-Like Nanostructure for Rechargeable Zinc-Air Batteries. *Chem. Eng. J.* **2022**, *429*, 132199. [CrossRef]
26. Wang, F.; Xiao, Z.; Liu, X.; Ren, J.; Xing, T.; Li, Z.; Li, X.; Chen, Y. Strategic design of cellulose nanofibers@zeolitic imidazolate frameworks derived mesoporous carbon-supported nanoscale $CoFe_2O_4$/CoFe hybrid composition as trifunctional electrocatalyst for Zn-air battery and self-powered overall water-splitting. *J. Power Sources* **2022**, *521*, 230925. [CrossRef]
27. Zhao, Y.; Zhang, L.; Qi, P.; Luo, H.; Lin, C.; Liu, W.; Zhang, D. Space-confined pyrolysis strategy to self-catalyze the growth of carbon nanotube-wrapped Co_3O_4 electrocatalyst for lithium-O_2 batteries. *J. Alloy. Compd.* **2022**, *905*, 164203. [CrossRef]
28. Etesami, M.; Nguyen, M.T.; Yonezawa, T.; Tuantranont, A.; Somwangthanaroj, A.; Kheawhom, S. 3D carbon nanotubes-graphene hybrids for energy conversion and storage applications. *Chem. Eng. J.* **2022**, *446*. [CrossRef]
29. Sun, J.; Zuo, Y.; Wang, H.; Shi, H.; Lu, S. Global-Local CNTs Conductive Network Couple with Co-Based Polyhedral Promotes the Electrocatalytic Reduction of Oxygen. *Catalysts* **2022**, *12*, 1508. [CrossRef]
30. Tang, J.; Salunkhe, R.R.; Liu, J.; Torad, N.L.; Imura, M.; Furukawa, S.; Yamauchi, Y. Thermal Conversion of Core–Shell Metal–Organic Frameworks: A New Method for Selectively Functionalized Nanoporous Hybrid Carbon. *J. Am. Chem. Soc.* **2015**, *137*, 1572–1580. [CrossRef]